Steady flows above a quartz crystal resonator driven at elevated amplitude

Rebekka König, Arne Langhoff, and Diethelm Johannsmann*
Institute of Physical Chemistry, Arnold-Sommerfeld-Strasse 4, D-38678 Clausthal-Zellerfeld, Germany
(Received 19 September 2013; revised manuscript received 30 December 2013; published 23 April 2014)

A steady flow of liquid was observed above the surface of a quartz crystal microbalance under conditions where the oscillation amplitude exceeded 10 nm. The streaming flow occurs parallel to the displacement vector and is directed towards the center of the plate. It is expected to have applications in acoustic sensing, in microfluidics, and in micromechanics in a wider sense. The flow is caused by the nonlinear term in the Navier-Stokes equation, which can produce a nonzero time-averaged force from a periodic velocity field. Central to the explanation are the flexural admixtures to the resonator's mode of vibration. Unlike pressure-driven flows, the acoustically driven steady flow attains its maximum velocity at a distance of a few hundred nanometers from the surface. It is therefore efficient in breaking bonds between adsorbed particles and the resonator surface. As a side aspect, the flow pattern amounts to a diagnostic tool, which gives access to the pattern of vibration. In particular, it leads to an estimate of the magnitude of the flexural admixtures to the thickness-shear vibration.

DOI: 10.1103/PhysRevE.89.043016 PACS number(s): 47.35.De, 43.25.+y, 83.85.Vb, 07.64.+z

I. INTRODUCTION

The quartz crystal microbalance (QCM) in recent years has seen an impressive evolution from a film thickness monitor [1] to a surface-analytical instrument with capabilities much beyond gravimetry [2]. The added information mostly originates from the analysis of the resonance bandwidth in addition to the resonance frequency and, also, from the comparison of the shifts of frequency and bandwidth between overtones. The increased depth of information has given access to samples which are much more complex than films [3]. Examples include vesicles [4], particles [5], droplets [6], (nano)bubbles [7], and biological cells [8]. While this progress certainly is impressive, it has also become clear that a further increase in the depth of information is highly desirable in those cases where the sample has a complicated structure. The added information might be obtained by combining the QCM with other surface-analytical techniques like ellipsometry [9] or electrochemical impedance spectroscopy [10], but it might also be obtained by exploiting a sensing dimension of the QCM, which has not been given much attention so far, namely, the variation of *oscillation amplitude*.

In exploiting high-amplitude effects, there are two different routes. The easier approach is to base the analysis on changes of frequency and bandwidth with amplitude [11]. Because of its inherent simplicity this method should be promising for the construction of sensors. Alternatively, one can study the consequences of high amplitudes using some other technique such as optical microscopy [12] or third-harmonic generation [13,14]. The work reported here relies on optical microscopy, which evidences a steady tangential flow. The effect is quantified and explained. The steady flow is relevant to the physics of the QCM in a number of different ways, elaborated on in the Discussion.

A dependence of resonance frequency on amplitude is well known from time and frequency control. Even bare resonators in vacuum display a so-called "drive level dependence," which goes back to a slight nonlinearity in the stress-chain relations of crystalline quartz [15,16]. For applications in time and frequency control, the drive level dependence mostly is a problem; there is little to be gained from it. In the context of sensing, an early experiment exploiting high amplitudes was reported by Cooper *et al*. [14]. These authors detached virus particles from a resonator surface by ramping up the amplitude. The critical amplitude for shake-off was the principal target of observation. The authors term this technique "rupture event scanning" (REVS). Along similar (but not identical) lines, Edvardsson *et al*. [12] and Heitmann *et al*. [17] performed experiments where the adsorption of particles and of biological cells was *prevented* by running the resonator at high amplitudes. Heitmann *et al*. report that some cells are more efficiently repelled from the resonator surface than others. This effect allows one to distinguish between different types of cells. It parallels a related effect occurring with conventional ultrasound (compressional waves) in the bulk. In Ref. [18], Petersson *et al*. show that lipid particles can be separated from erythrocytes by standing acoustic waves in a microfluidic environment, based on differences in density and compressibility. Whereas the underlying theory has been formulated for the bulk effects reported in Ref. [18], no such theory exists for cells being repelled from a QCM surface running at high amplitude. Edvardsson *et al*. emphasize that adsorption was irreversible in their experiments, once it had occurred. These authors attribute their observations to effects of fluid dynamics, as opposed to effects of contact mechanics. In making that claim, they reason that an insufficient bond strength cannot be at the core of the phenomenon because the oscillation should in this case also be able to break bonds which exist already. This was not observed in Ref. [12] (contrasting with Ref. [14]). If the repulsion is based on fluid dynamics, particles may escape from the repulsive forces by adsorbing onto the surface. In the work reported below, we corroborate this interpretation. We show experimentally and theoretically that there is a steady tangential flow above a resonator operated at high amplitudes. Figure 1 sketches the situation. The flow opposes particle adsorption because it stabilizes a liquid layer in the gap between the particle and the surface. A similar effect occurs in ball bearings. Detachment of particles can be

*Author to whom correspondence should be addressed: johannsmann@pc.tu-clausthal.de

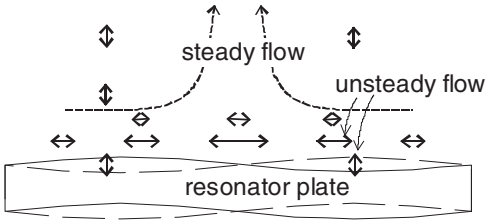

FIG. 1. The steady flow (dashed arrows) occurs parallel to the displacement direction. It is directed towards the center of the plate. Double arrows indicate oscillatory motion. Its normal component is independent of z because of incompressibility. Its tangential component decays within less than 1 μm. The combination of a normal oscillatory motion with a strong gradient in oscillatory tangential motion gives rise to steady forces.

expected to be less prominent than the prevention of particle adsorption.

Clearly, such flows have relevance beyond the immediate context of sensing. The QCM can act as a pump, similar to surface acoustic wave devices [19]. A small QCM might even be attached to objects floating on the water surface and propel these. The mechanism is similar to what is applied by "inertial squirmers" [20]. Quartz resonators (more generally, piezoelectric plates undergoing thickness shear and flexural motion at the same time) can take a role in microsystems technology.

II. MODELING

Nonlinear interactions between a quartz resonator and a sample come in two separate forms, which are either nonlinear mechanical effects or nonlinear fluid-dynamics effects. In contact mechanics, nonlinear force-displacement relations are ubiquitous because of the stress concentrations at the points of contact [11,21]. Most of them are in one way or another linked to the breaking or weakening of contacts under large loads. The nonlinear fluid-dynamics effects are of a different nature. They go back to the nonlinear term in the Navier-Stokes equation, also called the advected momentum term [22]. This latter nonlinearity is unrelated to materials properties. It is a consequence of the fact that momentum can be transported by convection. (There is a second source of nonlinearities in fluid dynamics, which is the fluid's finite compressibility [23]. Finite compressibility is of importance in gases. We disregard this set of nonlinearities here by approximating the medium as incompressible.)

The analytical model rests on a perturbation approach [22]. The velocity field is decomposed into a large unsteady part (a periodic motion at a few megahertz) and a small steady part. The Navier-Stokes equation applied to the unsteady component produces a nonzero time-averaged force, scaling as the square of the oscillation amplitude. The steady force density is much smaller than all oscillatory force densities because the Reynolds number is small. As we show, the force still suffices to set off a steady flow observable by the naked eye, if the amplitude of oscillation is a few tens of nanometers.

The Navier-Stokes equation is

$$\rho\left(\frac{\partial \mathbf{v}}{\partial t}+(\mathbf{v}\cdot\nabla)\,\mathbf{v}\right)=\eta\nabla^2\mathbf{v}-\nabla p+\mathbf{f}_{\text{body}}. \tag{1}$$

Bold letters denote vectors, $\mathbf{v}$ is the velocity, t is the time, ρ is the density, η is the viscosity, p is the hydrostatic pressure, and $\mathbf{f}_{\text{body}}$ is a density of body forces (for instance produced by gravity). We ignore body forces in the following. Applying perturbation theory, we decompose velocity and pressure into an unsteady part (index us) and a smaller steady part (index s) as

$$\begin{aligned}\mathbf{v}(\mathbf{r},t)&\approx \mathbf{v}_{us}(\mathbf{r})\cos[\omega t+\varphi(\mathbf{r})]+\mathbf{v}_s(\mathbf{r}),\\ p(\mathbf{r},t)&\approx p_{us}(\mathbf{r})\cos[\omega t+\varphi_p(\mathbf{r})]+p_s(\mathbf{r}).\end{aligned} \tag{2}$$

$\varphi(\mathbf{r})$ and $\varphi_p(\mathbf{r})$ are phases; $\mathbf{r}$ is position. In a first step, we consider the leading order only, that is, we apply the Navier-Stokes equation to the unsteady component. Replacing $\mathbf{v}$ and p in Eq. (1) by their unsteady parts, neglecting body forces, and slightly rearranging, we find

$$\begin{aligned}&-\rho\omega\mathbf{v}_{us}(\mathbf{r})\sin[\omega t+\varphi(\mathbf{r})]\\ &\approx -\rho[\mathbf{v}_{us}(\mathbf{r})\cdot\nabla]\mathbf{v}_{us}(\mathbf{r})\cos^2[\omega t+\varphi(\mathbf{r})]\\ &\quad+\eta\nabla^2\mathbf{v}_{us}(\mathbf{r})\cos[\omega t+\varphi(\mathbf{r})]-\nabla p_{us}(\mathbf{r})\cos[\omega t+\varphi_p(\mathbf{r})]\\ &=-\frac{\rho}{2}[\mathbf{v}_{us}(\mathbf{r})\cdot\nabla]\mathbf{v}_{us}(\mathbf{r})-\frac{\rho}{2}[\mathbf{v}_{us}(\mathbf{r})\cdot\nabla]\mathbf{v}_{us}(\mathbf{r})\\ &\quad\times\cos[2\omega t+2\varphi_p(\mathbf{r})]+\eta\nabla^2\mathbf{v}_{us}(\mathbf{r})\cos[\omega t+\varphi(\mathbf{r})]\\ &\quad-\nabla p_{us}(\mathbf{r})\cos[\omega t+\varphi_p(\mathbf{r})].\end{aligned} \tag{3}$$

Clearly, the left-hand side and the right-hand side in Eq. (3) cannot be strictly equal because the right-hand side contains terms at $\omega=0$ and 2ω. This follows from the fact that the advected momentum term is quadratic in velocity and, further, from the relation $\cos^2(x)=1/2[1+\cos(2x)]$. The time average of the first term on the right-hand side in Eq. (3) does *not* vanish. (The second-harmonic component at 2ω might have been included into the unsteady part of the flow field in Eq. (2). It is of a magnitude comparable to the steady component. Second-harmonic generation was disregarded for brevity.)

The first term on the right-hand side in Eq. (3) is small, which justifies the use of perturbation theory. The ratio of the terms $|\rho(\mathbf{v}_{us}\cdot\nabla)\mathbf{v}_{us}|$ and $|\eta\nabla^2\mathbf{v}_{us}|$ is assessed by the Reynolds number Re. To estimate Re, replace the gradients in Eq. (3) by the inverse penetration depth of the shear wave, δ^{-1}. δ is given as $\delta=(2\eta/[(\rho\omega)]^{1/2}$, which is 250 nm at 5 MHz in water. Further, approximate $|\mathbf{v}_{us}|$ by ωu_{us} with u_{us} the amplitude of oscillation. Using the estimates $u_{us}\approx 10$ nm, $\omega\approx 2\pi\times 5$ MHz, $\delta\approx 250$ nm, and $\eta\approx 10^{-3}$ Pa s, one arrives at $\text{Re}\approx\rho\omega u_{us}\delta/\eta\approx 0.05$.

In the following, we focus on the steady component. The Navier-Stokes equation applied to the steady flow is

$$\begin{aligned}0&\approx -\rho\langle[\mathbf{v}_{us}(\mathbf{r})\cdot\nabla]\mathbf{v}_{us}(\mathbf{r})\rangle_{\text{time}}+\eta\nabla^2\mathbf{v}_s(\mathbf{r})-\nabla p_s(\mathbf{r})\\ &=\mathbf{f}_s(\mathbf{r})+\eta\nabla^2\mathbf{v}_s(\mathbf{r})-\nabla p_s(\mathbf{r}).\end{aligned} \tag{4}$$

The angular brackets denote a time average. The term $-\rho\langle(\mathbf{v}_{us}\cdot\nabla)\mathbf{v}_{us}\rangle_{\text{time}}$ was renamed as $\mathbf{f}_s$ (a steady force density) in line 2. The left-hand side is zero because the time derivative of a steady quantity vanishes by definition. All terms which are

quadratic in small parameters [including the term $\rho(\mathbf{v}_s\cdot\nabla)\mathbf{v}_s$] were neglected. Clearly, the nonlinear term from Eq. (3) now acts as a source term, driving a steady second-order flow.

Importantly, there are symmetry constraints inherent to the structure of the source term. The source term contains a dot product. If the direction of the periodic flow and the gradient direction are perpendicular to each other, the dot product returns a zero and all steady flows become symmetry forbidden. If the periodic flow is a pure shear flow, the flow direction and the gradient direction *are* perpendicular to each other and steady flows consequently are not expected.

There are two separate reasons why the flow above a QCM surface deviates from a pure shear flow. First, the presence of particles distorts the shear flow. Particles were employed in Refs. [12,17] (and also in the work reported here). The particles experience a periodic rotation and a periodic translation at the same time. Synchronous rotation and translation give rise to a steady force directed towards the resonator surface [24]. The force can be thought of as being a high-frequency analog of the Magnus force [25]. There are characteristic differences between this force and the Magnus force, though [24]. A second difference between the flow above a QCM surface and a pure shear wave goes back to the flexural contributions to the vibration pattern of the plate [26]. Practical quartz crystal resonators all employ what is called "energy trapping." The amplitude of oscillation is large in the center of the plate and decays towards the edge. For reasons of volume conservation, an in-plane gradient in the amplitude of tangential motion causes an expansion or contraction of the material in the perpendicular direction, thereby inducing a motion normal to the surface. As discussed in more detail below Eq. (17), the size and direction of the normal component can be debated. For now, we write

$$v_{us,z}\,(z=0)=\alpha v_{us,x}\,(z=0)\,. \tag{5}$$

$v_{us,z}$ and $v_{us,x}$ are the amplitudes of the normal and the tangential components of the velocity. $z=0$ denotes the resonator surface, and α is a numerical factor. Note that $v_{us,z}$, $v_{us,x}$, and α depend on x and y; they are not constant over the resonator surface.

Steady tangential flows at a solid-liquid interface, which undergoes oscillation into both the tangential and the normal direction, were first described by Wang and Drachman [27]. For a more recent discussion, see Ref. [28]. The treatment by Wang and Drachman differs from the analysis presented here in that Wang and Drachman completely specify the geometry and rigorously solve the equations of fluid dynamics for the given geometry. More specifically, Wang and Drachman calculate the flow in a channel of finite width. Below, we rather rely on a separation of scales and make no assumption about the geometry of the liquid cell. Because we focus on a narrow spatial range (of width δ) close to the resonator surface, we can approximate the wavelength of compressional waves (which is much larger than δ) as infinite. By doing so, we neglect all effects of finite compressibility. Also, we assume $\nabla v_s \approx 0$ at $z \gg \delta$. (By doing so, we implicitly assume a cell thickness much larger than δ. This is the one assumption about the geometry of the cell.) $\nabla v_s \approx 0$ at $z \gg \delta$ can be only approximately true because constant velocity in the bulk of a closed liquid cell violates volume conservation. In reality, the flow generated by the resonator surface consists of convection rolls, but the size of the convection rolls much exceeds δ. The liquid is expected to flow towards the center of the plate close to the resonator surface and to flow in the reverse direction in the upper half of the cell. This pattern of motion is clearly evidenced in experiment. The height of the cell *does* have some influence on the velocity of the steady flow at the resonator surface. It has some influence because of the convection rolls and, also, because the upper window reflects compressional waves back to the crystal and thereby affects the normal component of the resonator's motion [29]. These influences acknowledged, the essential elements of the mechanism giving rise to the steady flow are captured by a model relying on a separation of scales and we proceed with modeling in this frame. There is a close connection between the flow field from Eq. (13) and what Sadhal calls the "inner solution" in Ref. [28]. Sadhal makes use of the stream function, which we avoid here.

To start out, we make simplifying assumptions. First, we assume incompressibility, with the consequence that the wavelength of conventional ultrasound, λ_{comp}, is much larger than the penetration depth of the shear wave. Second, we assume all in-plane gradients to occur on a length scale comparable to at least the thickness of the resonator plate, d_q. One might think that the in-plane gradients should occur on the scale of the width of plate, L, rather than the plate's thickness. However, we argue in the Discussion section that gradients also occur on the scale of the plate's thickness, which is less than L but still larger than δ. Since $\lambda_{\mathrm{comp}} \gg \delta$ we can neglect terms of the form $\partial v_{us,z}/\partial z$. Further, since $d_q \gg \delta$, all terms containing $\partial/\partial x$ can be neglected. Finally, we approximate the flow pattern as two dimensional (occurring in the xz plane, $v_{us,y} \approx 0$, $v_{s,y} \approx 0$). Making these approximations and spelling out the advected momentum term, the steady force density from Eq. (4), $\mathbf{f}_s$, is found to be

$$\begin{aligned}
f_{s,x} &= -\rho\langle(\mathbf{v}_{us}\cdot\nabla)v_{us,x}\rangle_{\mathrm{time}}\\
&= -\rho\left\langle v_{us,x}\frac{\partial v_{us,x}}{\partial x}+v_{us,z}\frac{\partial v_{us,x}}{\partial z}\right\rangle_{\mathrm{time}}\\
&\approx -\rho\left\langle v_{us,z}\frac{\partial v_{us,x}}{\partial z}\right\rangle_{\mathrm{time}},\\
f_{s,z} &= -\rho\langle(\mathbf{v}_{us}\cdot\nabla)v_{us,z}\rangle_{\mathrm{time}}\\
&= -\rho\left\langle v_{us,x}\frac{\partial v_{us,z}}{\partial x}+v_{us,z}\frac{\partial v_{us,z}}{\partial z}\right\rangle_{\mathrm{time}}\approx 0.
\end{aligned} \tag{6}$$

Clearly, the steady force is dominated by its x component. The steady flow mostly occurs parallel to the displacement direction.

The tangential component of the high-frequency velocity field (that is, of the decaying shear wave) is of the form

$$\begin{aligned}
v_{us,x}(z,t) &= v_S\mathrm{Re}\{\exp[i(\omega t-kz)]\}\\
&= v_S\mathrm{Re}\left\{\exp\left[i\left(\omega t-\frac{(1-i)z}{\delta}\right)\right]\right\}.\\
&= v_S\exp\left(-\frac{z}{\delta}\right)\cos\left(\omega t-\frac{z}{\delta}\right)
\end{aligned} \tag{7}$$

v_S is given as ωu_S with u_S the amplitude of oscillation at the resonator surface. (Capital S as an index denotes the sensor surface, not steady flow.) $k=k'-ik''$ is the complex wave

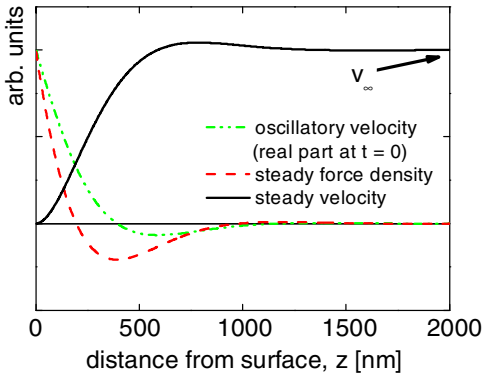

FIG. 2. (Color online) The z dependence of the oscillatory tangential velocity [$v_{us,x}(z,\, t = 0)$, dot-dashed, green, Eq. (7)], of the steady tangential force [$f_{s,x}(z)$, dashed, red, Eq. (10)], and of the steady velocity [($v_{s,x}(z)$, solid, black, Eq. (13)].

number. k' and k'' are both equal to δ^{-1} [30]. The real part of $v_{us,x}(z,t=0)$ is shown as a dash-dotted line in Fig. 2. A remark on terminology: Researchers from fluid dynamics do not consider decaying shear waves to be acoustic waves because shear waves do not propagate in liquids. They call those waves "boundary layers," which certainly makes sense. In calling them "acoustic shear waves," we follow the terminology used in the sensing community.

Since the wavelength of compressible waves was approximated as infinite, the normal component of the velocity field is independent of z:

$$v_{us,z}\,(z,t) \approx \alpha v_S \cos(\omega t)\,. \tag{8}$$

Again, α is a numerical coefficient discussed in more depth at the end of the Discussion section. The density of the steady force becomes

$$\begin{aligned} f_{s,x} &\approx -\rho \left\langle v_{us,z} \frac{\partial v_{us,x}}{\partial z} \right\rangle_{\text{time}} \\ &= -\rho\alpha v_S^2 \left\langle \cos(\omega t) \frac{\partial}{\partial z} \left[\exp\left(-\frac{z}{\delta}\right) \cos\left(\omega t - \frac{z}{\delta}\right) \right] \right\rangle_{\text{time}} \\ &= \frac{\rho\alpha v_s^2}{\delta} \exp\left(-\frac{z}{\delta}\right) \left\langle \cos(\omega t) \left(\cos\left(\omega t - \frac{z}{\delta}\right) \right.\right. \\ &\quad \left.\left. - \sin\left(\omega t - \frac{z}{\delta}\right) \right) \right\rangle_{\text{time}} . \end{aligned} \tag{9}$$

Performing the time average yields

$$\begin{aligned} f_{s,x} &\approx \frac{\rho\alpha v_S^2}{2\delta} \exp\left(-\frac{z}{\delta}\right) \left[\cos\left(\frac{z}{\delta}\right) + \sin\left(\frac{z}{\delta}\right) \right] \\ &= \frac{\rho\alpha\omega^2 u_S^2}{2\delta} \exp\left(-\frac{z}{\delta}\right) \left[\cos\left(\frac{z}{\delta}\right) + \sin\left(\frac{z}{\delta}\right) \right]. \end{aligned} \tag{10}$$

$f_{s,x}$ is shown as a dashed line in Fig. 2. The force acts parallel to the displacement direction. Whether it acts towards positive or negative x depends on the sign of α.

In order to find the steady velocity field $v_s(z)$, we insert Eq. (10) into Eq. (4). We expect a shear flow and therefore set p_s to zero. The equation to be solved is

$$\begin{aligned} \eta \frac{\partial^2 v_{s,x}(z)}{\partial z^2} &= -f_{s,x}(z) \\ &= -\frac{\rho\alpha\omega^2 u_S^2}{2\delta} \exp\left(-\frac{z}{\delta}\right) \left[\cos\left(\frac{z}{\delta}\right) + \sin\left(\frac{z}{\delta}\right) \right]. \end{aligned} \tag{11}$$

Formal integration yields

$$\begin{aligned} v_{s,x}(z) &= C_1 + C_2 z \\ &\quad - \frac{\delta\alpha\rho\omega^2 u_S^2}{4\eta} \exp\left(-\frac{z}{\delta}\right) \left[\cos\left(\frac{z}{\delta}\right) - \sin\left(\frac{z}{\delta}\right) \right]. \end{aligned} \tag{12}$$

C_1 and C_2 are integration constants, to be determined from the boundary conditions. The requirement of $\partial v_{s,x}\,(z)\,/\partial z = 0$ in the limit of $z \to \infty$ yields $C_2 = 0$. The no-slip condition at the resonator surface $[v_{s,x}(0) = 0]$ yields $C_1 = \delta\alpha\rho\omega^2 u_S^2/\,(4\eta)$. Inserting the integration constants into Eq. (12) leads to

$$\begin{aligned} v_{s,x}(z) &= \frac{\delta\alpha\rho\omega^2 u_S^2}{4\eta} \\ &\quad \times \left\{ 1 - \exp\left(-\frac{z}{\delta}\right) \left[\cos\left(\frac{z}{\delta}\right) - \sin\left(\frac{z}{\delta}\right) \right] \right\}. \end{aligned} \tag{13}$$

The flow profile is shown as a solid line in Fig. 2. The flow is a shear flow within about a range of twice the penetration depth and levels off towards to a constant velocity above that distance.

The velocity at large distances from the resonator surface ($z \gg \delta$) is

$$v_\infty = \frac{\delta\alpha\rho\omega^2 u_S^2}{4\eta} \tag{14}$$

For an estimate of v_∞, use the same values as before ($\delta \approx 250$ nm, $\rho \approx 10^3$ kg/m^3, $\omega \approx 2\pi \times 5$ MHz, and $\eta \approx 10^{-3}$ Pa s), leading to

$$v_\infty \approx 60 \frac{\mu\text{m}}{\text{s}} \alpha\, (u_S\ [\text{nm}])^2\,. \tag{15}$$

This leaves the question of what value should be used for α and this question actually is relevant beyond the immediate context of steady streaming. Flexural contributions to the vibration pattern of the so-called "thickness-shear resonators" have been known since the early days of acoustic sensing. At the time, thickness-shear resonators were *not* used for sensing in liquids because researchers believed that the flexural contributions would make meaningful measurements impossible. In their 1949 paper, Mason and co-workers desribe a rather intricate apparatus designed to measure the viscosity of complex fluids in the megahertz range. In the Introduction, they justify the effort and comment on why they did not directly immerse thickness-shear resonators into the fluid [31]. They write: "Consideration was given to the use of a thickness vibrating shear crystal of the AT or BT type, but it was found that the shear motion was too closely coupled to other modes of motion, such as flexure modes, to give reliable results. Hence another method had to be used."

Mason and co-workers certainly have a point, but the problem is not as severe as they thought. Given the relevance,

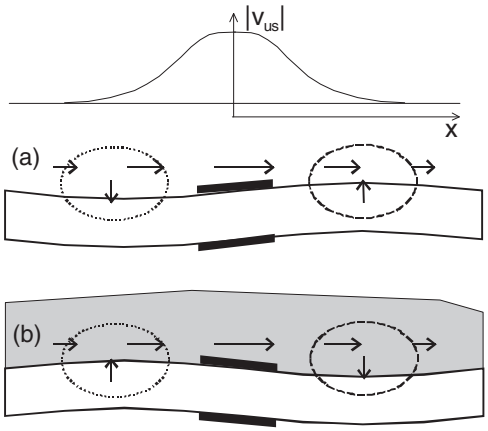

FIG. 3. Most practical "thickness-shear resonators" are designed such that the amplitude of oscillation is large in the center and decays towards the edge. The amplitude distribution is sketched at the top of (a). This distribution is achieved by making the plate slightly thicker in the center than at the edge, for instance with electrodes applied to the center only (thick black lines). For reasons of volume conservation (more precisely, because of the nonzero Poisson ratio), an in-plane gradient in the amplitude of tangential oscillation produces a periodic bending of the plate. In air, the plate bends convexly in regions where the gradient in tangential displacement would produce a compression [dashed line in (a)]. However, when the resonator is immersed in a liquid, a similar volume-conservation argument applies to the liquid phase. The liquid pushes the plate downwards because it resists compression, as well. The plate bends *downwards* for that reason (b).

we briefly remind the reader of energy trapping. In order to mount a thickness-shear resonator in a holder, the resonator must be configured such that the amplitude of oscillation is small at the point of contact with the holder. Otherwise, the holder overdamps the resonance. The solution widely employed is to make the plates slightly thicker in the center than at the rim. One can either employ convexly shaped crystals [32] or use planar crystals with sufficiently thick electrodes applied to the center of the plate only [33]. The resonator can be viewed as an acoustic cavity with curved surfaces. The curved surfaces focus the acoustic energy to the center. Figure 3(a) sketches a resonator in air. The thin line above panel (a) is the amplitude distribution of the tangential displacement. (This sketch ignores the rings of low amplitude discussed around Fig. 6.) If the motion were indeed of the thickness-shear type, the material would be compressed in the region encircled with a dashed line in panel (a); it would expand in the region encircled with a dotted line. Since the Poisson number is nonzero, the plate bends in order to lower the volume change. Finite element simulations show that the amplitude of the normal motion in the regions encircled in Fig. 3(a) can easily be a few times larger than the amplitude of motion in the tangential direction. In air, the parameter α from Eq. (5) is larger than 1 in the dashed region in Fig. 3(a) and smaller than -1 in the dotted region. If the resonator behaved in the same way in liquids, Mason and co-workers would have been correct in pointing out that the QCM does not operate as a thickness-shear device. It would mostly probe the liquid's compressional wave impedance rather than its shear wave impedance. Effects of compressional waves would be strong and the QCM would basically be useless (in liquids).

There are two complications, which Mason and co-workers did not sufficiently appreciate at the time. Both complications work to the advantage of gravimetric sensing in liquids. First, the liquid itself is subjected to the same contraction and expansion as the crystal. Second, the resonator is a rather soft device with regard to bending. While the resonator wants to bend upwards in the dashed region in Fig. 3, the liquid wants to expand downwards, and the liquid wins. The fact that the plate exposed to a liquid on one side (slightly) bends *downwards* in the dashed region is proven by the experiments reported below. In the following, we make the argument more quantitative.

The vertical displacement of the solid-liquid interface $u_z(x,y)$ results from a stress balance. By the principle of reaction, the stress exerted by the liquid onto the plate and the stress exerted in the reverse direction have to be equal and opposite. Both media respond with a normal stress to $u_z(x,y)$ being different from the equilibrium displacements of the respective free surfaces. We need to estimate these stresses. For the liquid, the normal stress σ_{zz} and the vertical displacement u_z are related to each other by the compressional wave impedance. One has

$$\begin{aligned}\sigma_{zz} &= Z_{\mathrm{comp,liq}}(v_z - v_{z,\mathrm{free,liq}}) \\ &= Z_{\mathrm{comp,liq}} i\omega(u_z - u_{z,\mathrm{free,liq}}).\end{aligned} \tag{16}$$

σ_{zz}, v_z, and u_z all are unsteady parameters. The index us was omitted for brevity. The compressional wave impedance $Z_{\mathrm{comp,liq}}$ is the ratio of normal stress and velocity. It is given as $Z_{\mathrm{comp,liq}} = \rho c$ with ρ the density and c the speed of sound. Using $\rho = 10^3$ kg/m^3 and $c = 1500$ m/s, one finds $Z_{\mathrm{comp,liq}} \approx 1.5 \times 10^6$ kg/(m^2 s). With $\omega = 2\pi \times 5$ MHz, the ratio of stress and displacement comes out as 4.5×10^{14} Pa/m.

For an elastic plate, normal stress and bending deformation are related to each other by the Euler-Bernoulli equation [34]

$$\sigma_{zz} \approx EI \frac{d^4(u_z - u_{z,\mathrm{free,plate}})}{dx^4}. \tag{17}$$

E is the Young's modulus and I is the second moment of the area. For the parallel plate, the second moment of the area is given as $I = d_q^3/12$ with d_q the thickness of the plate. d_q is equal to 330 μm for 5 MHz quartz resonators. Equation (17) applies to isotropic media. For the sake of an estimate, we approximate the effective Young's modulus of the quartz plate (which is anisotropic in reality) by the Young's modulus of silica, which is around 70 GPa. Also, we replace d^4/dx^4 by $1/L^4$ with L the width of the plate. For an estimate, use $L \approx 5$ mm. With these values, the ratio between normal stress and normal displacement comes out as 2.6×10^9 Pa/m, which is to be compared to 4.5×10^{14} Pa/m found for the liquid. Clearly, the plate is much softer with regard to normal displacements than the liquid. This is the essential step in the argument. The bending stiffness of the plate is too small to compete with the pressure exerted by the liquid. As a consequence, the vertical displacement eventually adopted is close to $u_{z,\mathrm{free,liq}}$. The plate bends *downwards*. Figure 3(b) (with the degree of bending much exaggerated) comes closer to the real situation than Fig. 3(a). The parameter α in Eq. (5) is negative and positive in the dashed ($x > 0$) and the dotted ($x < 0$) regions,

respectively. For that reason, the flow is directed towards the center. If the plate were to bend upwards in the dashed region in Fig. 3(a), the steady flow would be directed towards the edge, contradicting the experimental results.

III. EXPERIMENT

Experiments were performed with crystals having a fundamental frequency of 5 MHz and a diameter of 1 in., supplied by Maxtek Inc. (Santa Fe Springs, CA). The resonators were mounted in a home-built holder. The resonance was driven with an impedance analyzer, namely, the unit SA250B from Saunders (Phoenix, AZ). An amplifier (nominal amplification of 30 dB, ZHL–1–2W, Minicircuits, Brooklyn, NY) was inserted between the impedance analyzer OUT and the resonator to achieve amplitudes above 10 nm. An attenuator was inserted between the resonator and the analyzer IN in order not to overload the detector. In order to excite the steady flow, the resonator was either driven at the resonance frequency or frequency sweeps were undertaken, where the span of the sweeps was less than the bandwidth of the resonance, so that the resonator was on resonance all the time.

The amplitude of oscillation u_0 was estimated from the voltage at the electrodes U_{el}, using the relation [35]

$$u_0 \approx \frac{4}{(n\pi)^2} Q d_{26} U_{el}. \tag{18}$$

Q is the quality factor and $d_{26} = 3.1\times10^{-12}$ m/V is the piezoelectric strain coefficient of AT—cut quartz. The quality factor was around $Q = 3500$. n is the overtone order. Most experiments were undertaken on the fundamental ($n = 1$). Inserting values, we find $u_0 \approx 4.5$ (nm) $\times$ U_{el} (V). Again: Eq. (18) is an estimate because it is based on the theory of the parallel plate. Equation (18) ignores energy trapping.

All experiments occurred in water. The flow was visualized with polystyrene spheres with diameter of 10 μm (product code 01-00-104, supplied by Micromod Partikeltechnologie GmbH, Rostock, Germany) dispersed in the liquid. The flow can be observed by eye, albeit with some difficulty. For a refined analysis, a microscope and a video camera were employed. A video is supplied in the Supplemental Material [36]. The velocity was extracted from the video frames by determining particle positions and the shifts thereof over time. IMAGEJ (an image analysis software supplied by the NIH [37]) was used to calculate particle positions.

IV. RESULTS AND DISCUSSION

The flow pattern is shown in Fig. 1. At the resonator surface the flow occurs parallel to the crystallographic x axis (the displacement direction) and is directed towards the center of the plate. The x direction was determined with conoscopy as explained in the Appendix. The flow pattern consists of convection rolls. When adjusting the focal plane of the microscope to a level close to the resonator surface, one sees the particles moving inwards. The reverse flow is found in the upper part of the cell. Of course, the velocity is not everywhere the same, it depends on position (x and y). The quantitative analysis was based on the fast particles.

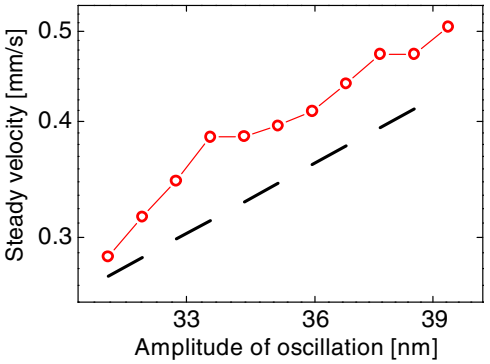

FIG. 4. (Color online) Velocity of the steady flow versus oscillation amplitude as determined from a video of the flow (see Supplemental Material [36]). The cell height was 5 mm. The data are compatible with a quadratic scaling of velocity with amplitude (dashed line).

Figure 4 shows a selected data set of velocity versus amplitude in double-logarithmic form. The amplitude of oscillation was calculated from Eq. (18). The velocity increases with amplitude, and the increase is compatible with quadratic scaling as indicated by the solid line. The velocity of the steady flow was found to depend on the thickness of the cell; the spread in velocities measured for the different heights amounted to about a factor of 2 (data not shown). Such a dependence is not covered by the theoretical analysis above, but it is not surprising, given the assumptions entering the derivation.

Figure 5 shows the comparison between overtone orders. Clearly, there is a dependence on overtone order n. A theoretical explanation of this dependence is difficult, because it is not clear how the parameter α (the amplitude of the flexural components, normalized to the amplitude of tangential motion) depends on overtone order. For all parameters entering Eq. (14) other than α, the dependence on overtone order is known. The product of these other factors leads to a scaling of $n^{-3/2}$ as shown by the dashed line. The fact that v_∞/α scales as $n^{-3/2}$ follows from the combination of Eq. (14) and Eq. (18). According to Eq. (14), we have $v_\infty/\alpha \sim n^2\delta u_S^2$. With $\delta = [2\eta/(\rho\omega)]^{1/2} \sim n^{-1/2}$, this amounts to $v_\infty/\alpha \sim n^{3/2}u_S^2$. Following Eq. (18), we have $u_S \sim n^{-2}QU_{el}$. The quality factor Q is given as $f_r/(2\Gamma)$ with f_r the resonance frequency (scaling as n) and Γ the half width at half maximum, scaling as $n^{1/2}$ [38]. Q therefore scales as $n^{1/2}$. We arrive at $u_S \sim n^{-3/2}U_{el}$,

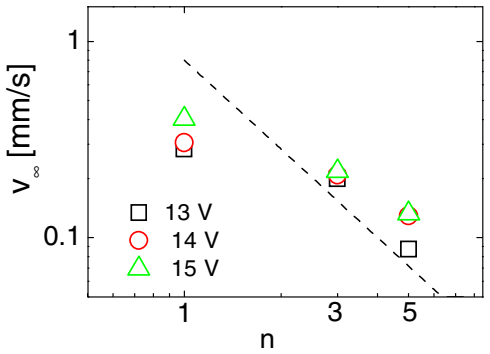

FIG. 5. (Color online) Comparison of the steady velocities between overtone orders. The dashed line denotes a power law of $n^{-3/2}$.

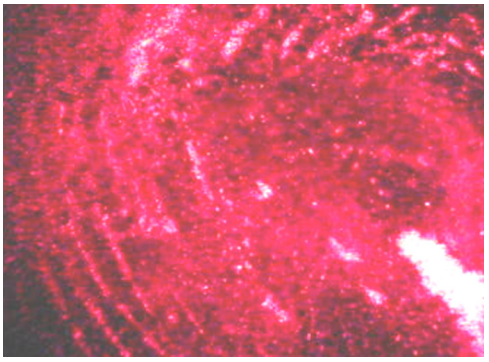

FIG. 6. (Color online) In some case, particles were found to deposit in ring-shaped areas, where the distance between the rings was about twice the thickness of the crystal. The particles used to produce the above image were glass spheres with a diameter of 5 μm. The light source was a helium-neon laser, hence the red color. The amplitude of oscillation was 32 nm. The rings developed after the resonator had been driven at this amplitude for about an hour. Tentatively, they are explained as areas of lower-than-average amplitude. The width of the image corresponds to 10 mm.

which after insertion into Eq. (14) leads to $v_\infty/\alpha \sim n^{-3/2}$. From the fact that the data in Fig. 5 do not follow the dashed line, one concludes that α itself depends on overtone order.

Steady streaming can also serve as a diagnostic tool. It carries information on the vibration pattern of the resonator. There are three different aspects to this approach.

While symmetry predicts that the line of stagnant flow should be in the center of the resonator, this was not usually the case. The flow pattern was asymmetric. Clearly, the crystals employed were significantly nonideal. The origins of this behavior are unclear. Reasons for the asymmetry might be the anchors of the electrodes, but also crystal defects, which are not optically visible. Such irregularities are also seen in Fig. 5 of Ref. [39]. Steady streaming can be employed to check for crystal imperfections. A good crystal will show a symmetric flow pattern.

We sometimes find rings of deposited particles. An example is shown in Fig. 6. Similar rings are visible in Fig. 5 of Ref. [39] and also in Fig. 4 of Ref. [40]. We interpret these as areas of lower-than-average oscillation amplitude. The spacing between the rings is about twice the crystal thickness. Such rings are not captured by the widely employed theory of energy trapping based on the work by Tiersten [32]. They *are* captured, at least implicitly, in Ref. [33]. One can think of the ring-shaped pattern in Fig. 6 as a diffraction pattern. It is caused by diffraction of the plane shear wave at the edge of the electrode. The characteristic features size of such patterns is the wavelength, which is of the order of $2d_q$ with d_q the thickness of the plate.

Flexural contributions to the mode of vibration are typically associated with energy trapping. However, we also found steady streaming for crystals which did not employ energy trapping. These resonators had electrodes covering the entire surface on both sides. Such resonators can be mounted with soft pads of silicone [41]. The electrical contact occurred with thin wires, glued to the edge of the electrodes. While one might think that this scheme avoids flexural contributions and compressional waves, the experiment evidences the opposite (data not shown). These resonators induced steady streaming as well, which proves the presence of compressional waves. For a numerical analysis of this problem see Ref. [42].

Figure 4 allows for an estimate of the magnitude of α. Comparing the values of v_∞ from Fig. 4 to the prediction from Eq. (15), one finds values of α of around 0.1. Friedt and co-workers came to a similar conclusion, combining the QCM with an atomic force microscope [43].

Without going into the details, we briefly discuss what might be viewed as an inconsistency at first glance. We argued in the modeling section that the QCM in a liquid deserves this name because the effects of the flexural contributions are small. Because the compressional wave impedance of liquids is large (larger than the shear wave impedance by at least a factor of 10^2), one might think that $\alpha \approx 0.1$ is not small in this sense. According to the small-load approximation [3] the frequency shift and the acoustic wave impedance are linearly related. Since the compressional wave impedance is much larger than the shear wave impedance, one can expect a 10% contribution of normal motion to the displacement pattern to induce very significant shifts of the resonance frequency. The effects of compressional waves should be *larger* than the effects of shear waves. However, this contradicts experimental experience. The viscosities of simple liquids like water as determined by the QCM are not grossly wrong [38,44]. The seemingly contradictory situation arises because the small-load approximation does *not* apply to the flexural modes. The latter statement is a consequence of the very argument outlined above. The large bulk modulus of the liquid constrains the flexural modes to be small and—at the same time—invalidates the small-load approximation. Compressional waves are not a small load and therefore—somewhat surprisingly—have a smaller effect on the frequency shift than simple-minded estimates would predict.

We conclude by pointing out a peculiarity of the acoustically driven flow, which is that the maximum velocity occurs close to the surface. $v_{s,x}(z)$ reaches its limiting value of v_∞ at a distance from the surface of less than 1 μm (see Fig. 2). The same is true for flows driven by surface acoustic waves [45] and for electro-osmotic flows [46] but not for pressure-driven flows, which have a parabolic profile. Large velocities at the sensor surface are a benefit for sensing because they speed up the convective transport of analytes to the sensor surface. Typically, the time resolution achievable in kinetic adsorption experiments is limited by the diffusion of the analyte through the Nernst layer [47]. The time resolution can be improved by suitable design of the sensor and the hydrodynamic boundary conditions. Another option is to choose a type of flow which is fast right at the surface. Such a flow can be produced above a QCM with a quick pulse of high amplitude. It should also be efficient in removing virus particles adsorbed to a sensor surface. This mechanism needs attention when analyzing REVS experiments [14].

V. CONCLUSIONS

Quartz crystal resonators employing energy trapping and oscillating at an amplitude above 10 nm produce a steady tangential flow towards the center of the plate, parallel to the displacement direction. The flow is the consequence of the

flexural contribution to the plate's mode of vibration. The flow can be used to pump liquids, to detach particles, and to prevent particle adsorption. It should also be of use for particle sorting. The effect is strongest on the fundamental. Its magnitude allows for an estimate of the magnitude of the flexural admixtures to the vibration pattern.

ACKNOWLEDGMENT

Technical help by A. Böttcher is gratefully acknowledged.

APPENDIX: DETERMINATION OF THE CRYSTALLOGRAPHIC *x* AXIS WITH A POLARIZING MICROSCOPE

For most sensing applications of a QCM, the displacement direction is irrelevant. All that matters are shifts of frequency and bandwidth. Steady streaming is one of the few exceptions. The x axis of the crystal must be known in order to predict the direction of flow.

There are crystals on the market which are truncated at one side, where the flat part denotes the x axis [Fig. 7(a)]. However, the crystals used here do not have this kind of truncation and the crystallographic axes therefore are unknown. For such crystals, a polarizing microscope equipped with a conoscopy module (a "Bertrand lens") can help [48]. In conoscopy, the pixels on the screen correspond to beams passing through the sample under different *angles*. One usually employs crossed polarizers and studies birefringent samples. Since quartz is uniaxially birefringent, its conoscopic image displays colored rings [Fig. 7(b)]. The center of these rings is the optical axis, which is the crystallographic z axis. For the AT cut, the z axis is inclined away from the surface normal by 55°. With the numerical apertures typically employed, the center of the colored rings is outside the field of view, but one can still infer the orientation of the x axis from the rings as indicated in Fig. 7(c). Depending on the orientation of the crystal relative to the polarizers, the conoscopic image may display black lines. These are the arms of a Maltese cross, which is centered on the optical axis. Again, the center of the cross is not usually inside the field of view, but one can infer its location (more precisely, its orientation) by rotating the sample and watching the movement of the arms of the cross.

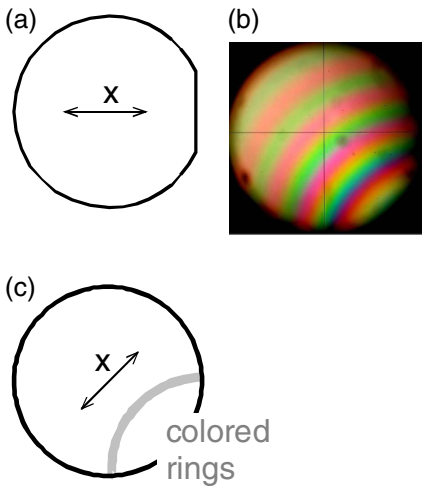

FIG. 7. (Color online) Determination of the crystallographic x axis by conoscopy. (a) Some crystals have a flat part at the edge, indicating the direction of the x axis. (b),(c) For round crystals, the crystallographic x axis can be found with a polarizing microscope, using the conoscopic mode. One observes colored rings. The z axis corresponds to the center of these rings. (c) shows the direction of the x axis. The radius of the field of view in (b) corresponds to about 30°.

[1] C. Lu and A. W. Czanderna, *Applications of Piezoelectric Quartz Crystal Microbalances* (Elsevier, Amsterdam, 1984).

[2] *Piezoeletric Sensors*, edited by C. Steinem and A. Janshoff (Springer, Heidelberg, 2007).

[3] D. Johannsmann, Phys. Chem. Chem. Phys. **10**, 4516 (2008).

[4] C. A. Keller and B. Kasemo, Biophys. J. **75**, 1397 (1998).

[5] M. Berglin, A. Olsson, and H. Elwing, Macromol. Biosci. **8**, 410 (2008).

[6] L. McKenna, M. I. Newton, G. McHale, R. Lucklum, and J. Schroeder, J. Appl. Phys. **89**, 676 (2001).

[7] X. H. Zhang, Phys. Chem. Chem. Phys. **10**, 6842 (2008).

[8] V. Heitmann, B. Reiss, and J. Wegener, in *Piezoelectric Sensors* (Ref. [2]).

[9] E. Sabatani, E. Ticianelli, A. Redondo, I. Rubinstein, J. Rishpon, and S. Gottesfeld, Synth. Met. **55**, 1293 (1993).

[10] A. Sabot and S. Krause, Anal. Chem. **74**, 3304 (2002).

[11] S. Berg and D. Johannsmann, Phys. Rev. Lett. **91**, 145505 (2003).

[12] M. Edvardsson, M. Rodahl, and F. Hook, Analyst **131**, 822 (2006).

[13] S. K. Ghosh, V. P. Ostanin, and A. A. Seshia, Anal. Chem. **82**, 3929 (2010).

[14] M. A. Cooper, F. N. Dultsev, T. Minson, V. P. Ostanin, C. Abell,and D. Klenerman, Nat. Biotechnol. **19**, 833 (2001).

[15] J. Nosek, IEEE Trans. Ultrason. Ferroelectr. Freq. Control **46**, 823 (1999).

[16] H. F. Tiersten and D. S. Stevens, J. Acoust. Soc. Am. **80**, 1122 (1986).

[17] V. Heitmann, J. Wegener, Anal. Chem. **79**, 3392 (2007).

[18] F. Petersson, A. Nilsson, C. Holm, H. Jonsson, and T. Laurell, Analyst **129**, 938 (2004).

[19] T. M. Squires and S. R. Quake, Rev. Mod. Phys. **77**, 977 (2005).

[20] S. Wang and A. Ardekani, Phys. Fluids **24**, 101902 (2012).

[21] V. L. Popov, *Contact Mechanics and Friction: Physical Principles and Applications* (Springer, Heidelberg, 2010).

[22] H. Bruus, Lab Chip **12**, 20 (2012).

[23] N. Riley, Annu. Rev. Fluid Mech. **33**, 43 (2001).

[24] A. Langhoff and D. Johannsmann, Phys. Rev. E **88**, 013001 (2013).

[25] G. K. Batchelor, *An Introduction to Fluid Dynamics* (Cambridge University Press, Cambridge, 1967).
[26] W. J. Spencer and R. M. Hunt, J. Acoust. Soc. Am. **39**, 929 (1966).
[27] C. Y. Wang and B. Drachman, Appl. Sci. Res. **39**, 55 (1982).
[28] S. S. Sadhal, Lab Chip **12**, 2292 (2012).
[29] Z. X. Lin and M. D. Ward, Anal. Chem. **67**, 685 (1995).
[30] See, for instance, D. Johannsmann, in *Piezoeletric Sensors* (Ref. [2]).
[31] W. P. Mason, W. O. Baker, H. J. McSkimin, and J. H. Heiss, Phys. Rev. **75**, 936 (1949).
[32] H. F. Tiersten and R. C. Smythe, J. Acoust. Soc. Am. **65**, 1455 (1979).
[33] R. D. Mindlin and H. Deresiewicz, J. Appl. Phys. **25**, 21 (1954).
[34] J. M. Gere and S. P. Timoshenko, *Mechanics of Materials* (PWS Publishing Company, Brooks/Cole, 1997).
[35] D. Johannsmann and L. O. Heim, J. Appl. Phys. **100**, 094505 (2006).
[36] See Supplemental Material at http://link.aps.org/supplemental/10.1103/PhysRevE.89.043016 for a video showing the steady flow.
[37] http://rsb.info.nih.gov/ij/.
[38] C. D. Stockbridge, in *Vacuum Microbalance Techniques*, 4th ed., edited by K. H. Behrndt (Plenum, New York, 1966), Vol. 5.
[39] C. Hess, K. Borgwarth, and J. Heinze, Electrochim. Acta **45**, 3725 (2000).
[40] M. Edvardsson, P. Zhdanov, and F. Hook, Small **3**, 585 (2007).
[41] H. Ogi, K. Motohisa, K. Hatanaka, T. Ohmori, M. Hirao, and M. Nishiyama, Biosensors Bioelectronics **22**, 3238 (2007).
[42] http://www.comsol.com/model/download/177395/models.mems.thickness_shear_quartz_oscillator.pdf
[43] J. M. Friedt, K. H. Choi, L. Francis, and A. Campitelli, Jpn. J. Appl. Phys., Part 1 **41**, 3974 (2002).
[44] A. P. Borovikov, Instrum. Exp. Tech. **19**, 223 (1976).
[45] A. Wixforth, C. Strobl, Ch. Gauer, A. Toegl, J. Scriba, and Z. v. Guttenberg, Anal. Bioanal. Chem. **379**, 982 (2004).
[46] H. A. Stone, A. D. Stroock, and A. Ajdari, Annu. Rev. Fluid Mech. **36**, 381 (2004).
[47] T. M. Squires, R. J. Messinger, and S. R. Manalis, Nat. Biotechnol. **26**, 417 (2008).
[48] N. H. Hartshorne and A. Stuart, *Crystals and the Polarizing Microscope* (Hodder & Stoughton Educational, London, 1970).